



TECHNICAL ARTICLE

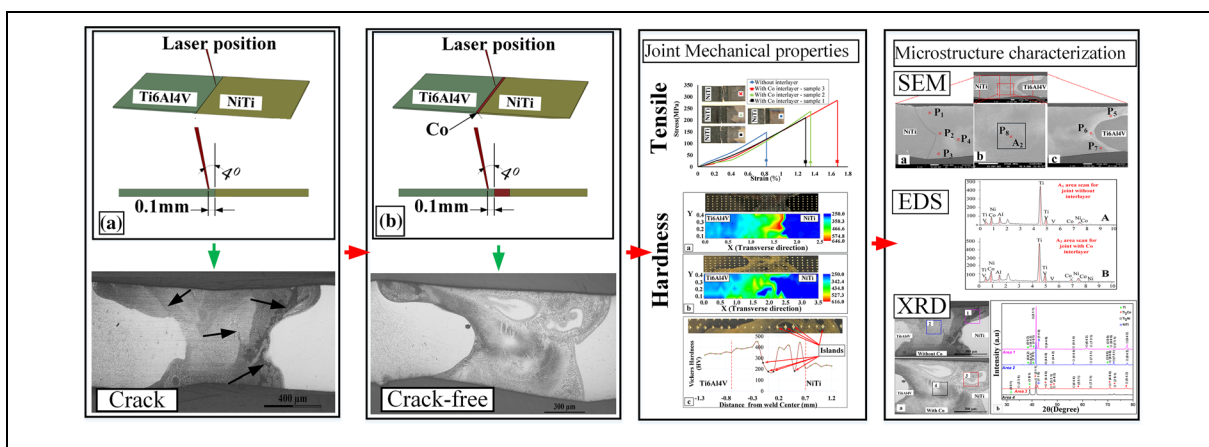
Microstructure, Macrosegregation, and Mechanical Properties of NiTi to Ti6Al4V Dissimilar Laser Welds Using Co Interlayer

Fissha Biruke Teshome, Bei Peng, J.P. Oliveira, Sansan Ao, Wenchao Ke, Fuguo Ge, and Zhi Zeng

Submitted: 26 January 2022 / Revised: 15 April 2022 / Accepted: 10 May 2022 / Published online: 27 June 2022

Joining alloys exhibiting individual superior properties could yield major benefits in terms of design and production flexibility. Nevertheless, differences in thermophysical properties between the materials to be joined complicate the formation of dissimilar combinations, thus limiting the potential applications of multiple engineering alloys. The formation of brittle Ti_2Ni intermetallic (IMC) in the fusion zone (FZ) is the main challenge in joining NiTi to Ti6Al4V without an interlayer. Hence, the composition of the FZ needs to be changed to ideally suppress brittle IMC phases to form and decrease the likelihood of crack formation upon solidification. In this study, two strategies were used concurrently to reduce brittle Ti_2Ni intermetallic compound: a cobalt interlayer was introduced in a butt joint configuration, and the laser was offset to the Ti6Al4V side. The use of a Co interlayer resulted in a joint free of brittle interaction layer susceptible to microcracks at the NiTi boundary by reducing the amount of brittle Ti_2Ni intermetallic compound. A joint with a lower hardness of 438HV was attained, compared to 515HV for the conventional NiTi/Ti6Al4V joint. The maximum strength and fracture strain of the Co-interlayered joint were improved to 285MPa and 1.67%, respectively, compared to 148MPa and 0.8% for the Co-free joint.

Graphical Abstract



Keywords cobalt interlayer, intermetallic, macrosegregation, microstructure, mechanical properties, NiTi, Ti6Al4V dissimilar laser welding

Fissha Biruke Teshome, Bei Peng, Wenchao Ke, and Fuguo Ge, School of Mechanical and Electrical Engineering, University of Electronic Science and Technology of China, Sichuan 611731, China; J.P. Oliveira, UNIDEMI, Department of Mechanical and Industrial Engineering, NOVA School of Science and Technology, NOVA University Lisbon, 2829-516 Caparica, Portugal; and CENIMAT/I3N, Department of Materials Science, NOVA School of Science and Technology, Universidade NOVA de Lisboa, 2829-516 Caparica,

Portugal; Sansan Ao, School of Material Science and Engineering, Tianjin University, Tianjin 300072, China; and Zhi Zeng, School of Mechanical and Electrical Engineering, University of Electronic Science and Technology of China, Sichuan 611731, China; and Institute of Electronic and Information Engineering of UESTC in Guangdong, Chengdu 523808, China. Contact e-mails: fishbiruke@gmail.com, beipeng@uestc.edu.cn, jp.oliveira@fct.unl.pt, ao33@tju.edu.cn, ke@std.uestc.edu.cn, gfg18200141721@163.com, zhizeng@uestc.edu.cn.

1. Introduction

Shape memory alloys (SMAs) are smart functional materials, which show unique properties of shape memory effect (SME) and superelasticity (SE) (Ref 1). These unique behaviors result from a solid-solid phase transformation between martensite and austenite phases, which can be actuated by stress, temperature or in the presence of a magnetic field (Ref 2). The functional properties of NiTi allow for a wide range of applications in a variety of industries. Among these industries, biomedical, aerospace, and micro-electro-mechanical-systems (MEMS) are potential applications for NiTi (Ref 3-5). Ti6Al4V is the most used titanium alloy with advantageous properties such as high strength-to-density ratio, corrosion resistance, and biocompatibility, which makes it attractive for the biomedical, automotive, and aerospace industries (Ref 6, 7). It would be ideal to successfully join these two materials in order to benefit from their distinct advantages at the same time. However, differences in thermophysical properties and the subsequent formation of brittle intermetallic (IMC) compounds, significant segregation, and the presence of high residual stresses pose several limitations when fusion welding of these dissimilar alloys is attempted (Ref 8). The Ti₂Ni and Ni₃Ti brittle IMC phases are easily formed during dissimilar welding of NiTi to Ti6Al4V (Ref 8-11), and they have been shown to cause mechanical property degradation and crack formation (Ref 11-16).

As of now, brazing, diffusion bonding, laser welding, friction stir welding, and ultrasonic spot welding were the major approaches attempted to join NiTi to Ti6Al4V alloys (Ref 17-20). Regarding laser welding of NiTi to Ti6Al4V, Miranda et al. (Ref 11) investigated the weldability of NiTi to Ti6Al4V with variable laser output powers and welding speeds, which resulted in FZ cracking in all trials. SEM analysis of the fractured surfaces revealed the presence of brittle Ti₂Ni, which was caused by nickel migration to the liquid Titanium. Zoeram and Mousavi (Ref 12, 21) investigated the effect of incorporating copper as an interlayer during laser welding of NiTi to Ti6Al4V and found that the copper interlayer improved the mechanical properties of the joint by reducing the amount of Ti₂Ni while introducing new Cu-based IMCs such as Ti₂Cu, Cu₂Ti, Cu₃Ti, and Cu₄Ti. Oliveira et al. (Ref 5) combined two strategies to control the formation of IMCs: i) offsetting the laser to the Ti6Al4V side and ii) applying niobium as an interlayer to create a sound NiTi/Ti6Al4V joint. The results showed that the Nb partially melted alongside with the Ti6Al4V while forming a eutectic with NiTi. Gao et al. (Ref 22) used a similar method and was successful in avoiding the formation of IMCs in laser welding Ti6Al4V to Inconel 718. Furthermore, several researchers have proposed using a filler metal with a higher ultimate tensile strength to mitigate IMC-induced brittleness in NiTi/Ti6Al4V joints by preventing or reducing IMCs formation in the FZ (Ref 2, 5, 12, 23). Zirconium, molybdenum, tantalum, tungsten, vanadium, silver, nickel, iron, and cobalt are examples of materials that could be used as an interlayer in a NiTi/Ti6Al4V joints (Ref 2, 9, 24-26), but the effect of these interlayers on laser welded NiTi and Ti6Al4V has not been investigated to the best of the authors' knowledge. In this study, cobalt was the material of interest as the interlayer.

Co has complete solubility with Ni in both the liquid and solid phases and is expected to discover a way to stop Ni

migration to Ti (Ref 27). Co is known to form Ni-Ti-Co SMA (Ref 28, 29), to preferentially enter Ni-sites (Ref 24), and to have a solid solution strengthening effect in Ti- and Ni-based alloys (Ref 30, 31). Co is known to be biocompatible aside from possessing excellent corrosion resistance (Ref 32, 33), superior tensile strength (1090 MPa), relatively high melting point (1495 °C), and high ductility (Ref 34). These properties make Co as a potential choice of interest as an interlayer to aid in joining NiTi to Ti6Al4V. Hence, laser offsetting and a Co interlayer were used to control the development of Ti₂Ni IMC in a NiTi/Ti6Al4V joint, and the impact on the microstructure, mechanical properties, and compositional change in the dissimilar welds was investigated.

2. Materials and Experiments

2.1 Materials and Preparation

The materials used in this study are austenitic NiTi (at room temperature), commercially available Ti6Al4V sheets, and 99.9 % purity cobalt foils with thicknesses of 30, 50, and 70 μm . The nominal composition of the NiTi and Ti6Al4V base materials is listed in Table 1. The as-received materials were machined to a size of 30 \times 30 \times 0.5 mm, and the faying surfaces were mechanically polished with a series of SiC papers to 1000 grits to ensure proper joint fit-up and remove the surface oxide. Furthermore, the samples were cleaned and degreased ultrasonically in an Acetone bath for 5 minutes, rinsed in distilled water, and dried thoroughly in the air before laser welding.

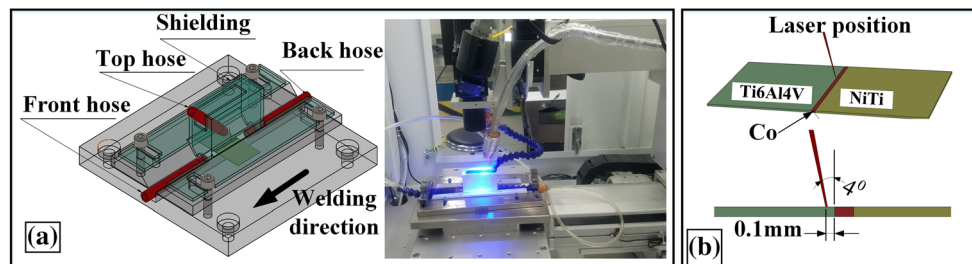
2.2 Laser Welding

An appropriate fixture with shielding aid, shown in Fig. 1(a), was designed to fix the workpieces and ensure an intense and continuous supply of argon to the fusion zone aiming at minimizing the joint oxidation. The welding experiments were performed using a fiber laser welding machine (LWF150QC from Wuhan HG Laser Engineering Co., Ltd.) with maximum operating peak power of 1500 W in both continuous and pulsed mode, a minimum focusing spot of 0.2~0.4 mm and wavelength of 1070 nm. Welding parameters employed were peak power: 1 kW, pulse frequency: 7 Hz, welding speed: 3 mm/sec, defocusing: 0 mm, argon flow rate: 17 L/hr and a ramped pulse profile with a total width of 13 ms. The laser process parameters were designed in a way to create spot overlap to achieve a continuous weld. Offsetting the laser to the NiTi side or keeping it at the center increases the amount of melted NiTi base material in the fusion zone, thus supplying a large amount of Ni to the fusion zone. In theory, controlling nickel movement into liquid titanium would be advantageous because it would reduce the formation of brittle Ti₂Ni. To accomplish this, the laser was placed on the Ti6Al4V side (as shown in Fig. 1(b), which is less susceptible to deterioration of its properties at high temperatures than NiTi).

Furthermore, the laser was offset from the cobalt boundary by 0.1 mm to the Ti6Al4V side to deliver more heat to this relatively high melting point material. Figure 1(b) illustrates a schematic of the set-up used for the laser welding procedure. As illustrated in Fig. 1(b), the Co interlayer was assembled in a butt configuration between the NiTi and Ti6Al4V sheets.

Table 1 Nominal material composition of the base materials

Base metal	Nominal compositions (at.%)								
	Ti	Ni	Al	V	Fe	C	N	H	O
NiTi	49.2	50.8
Ti6Al4V	Bal.	...	6.05	3.9	0.15	0.02	0.006	0.004	0.12

**Fig. 1** (a) Schematic of the fixture and setup of shielding gas nozzles and (b) Base material setup and laser positioning

Furthermore, the laser source was tilted by 4 degrees to protect the lenses from being damaged by the reflected beam.

2.3 Microstructural Characterization

Preparation of samples for microstructure characterization started from wire cutting series of transverse cross sections from the weld specimens. These samples were mounted on epoxy resin, ground on series of SiC papers from 80 to 2500 grit and polished with series of diamond pastes (0.05- 0.3 μm). After polishing, samples were immersed in distilled water, washed with alcohol, and dried before etching. As per the ASTM-E407-07-2015 standard, an etching mixture of 10ml HF, 25ml HNO_3 , and 150ml distilled water was employed to reveal the joint microstructure. ZEISS Observer A1M inverted optical microscope (OM) and JEOL JSM-7600F field emission scanning electron microscope (SEM) equipped with energy-dispersive spectroscopy (EDS) were employed to visualize transverse section microstructure and investigate the microstructure and chemical composition of the weld. The phases present in the weld were identified using x-ray diffraction (XRD, BRUKER D8 DISCOVER Plus) at 40 kV and 40 mA, using $\text{Cu-K}\alpha$ radiation.

2.4 Mechanical Tests

A digital microVickers hardness tester (DHV-1000 / DHV-1000Z) was used to measure the microhardness across the joint following the ASTM E384 (2008) standard. The indents were made with a load of 200g, a 10 second holding time, and each indentation was spaced by 100 μm in the longitudinal direction and 70 μm in the transverse direction, as detail in Fig. 2. The microhardness map was extended between the base materials through the weld fusion zone.

Tensile testing samples with 30 mm gage length (as shown in Fig. 2 b) were prepared from the central portion of the weld using wire-cut electrical discharge machining. Tensile testing was done at room temperature following the ASTM-E8-M and ASTM F2516-07 standards on a universal microtensile testing machine (CMT-02) with an accuracy of $\pm 0.5\mu\text{m}$ and a constant

cross-head displacement of 0.5 mm/min. Furthermore, SEM was used to visualize the fracture surfaces.

3. Results and Discussion

3.1 Microstructure of Weld

3.1.1 Microstructure of NiTi/Ti6Al4V Joint with and without Co Interlayer. Figure 3 depicts the cross section of the dissimilar joint obtained without addition of the Co interlayer. The weld pool had a broader width on top of the Ti6Al4V side, the reason being that the laser was tilted by 4° to the vertical and offset by 0.1 mm from the cobalt boundary toward the Ti6Al4V side. Identical welding conditions were used in both un-interlayered and Co-interlayered NiTi/Ti6Al4V welds.

Several previous studies have found that direct laser welding between NiTi and Ti6Al4V results in a weaker joint prone to premature failure, as well as a brittle interaction layer susceptible to microcracks within the fusion zone (Ref 11, 35). Microcracks near the NiTi side of the fusion zone are mainly caused by the formation of brittle Ti-Ni phases (especially Ti_2Ni) and the significant differences in the thermophysical properties of the two base materials (Ref 5, 12). Similar microstructural features were observed on the NiTi/Ti6Al4V joint micrographs (A, C, and D), which revealed the presence of an interaction layer serving as an initiation site for a network of cracks on the NiTi boundary.

The amount of Co introduced will have a significant impact on the joint's mechanical properties. As a result, a preliminary investigation was carried out to determine the appropriate interlayer thickness among 30, 50, and 70 μm thick Co foils, and the resulting microstructure at the NiTi boundary and the fusion zone is depicted in Fig. 4. According to preliminary test results presented in Fig. 4(d), the joint with a 50 μm thick Co interlayer has the best mechanical performance, while the joint with a 30 μm thick Co interlayer has the worst. As a result, the sections that follow present an in-depth investigation into the

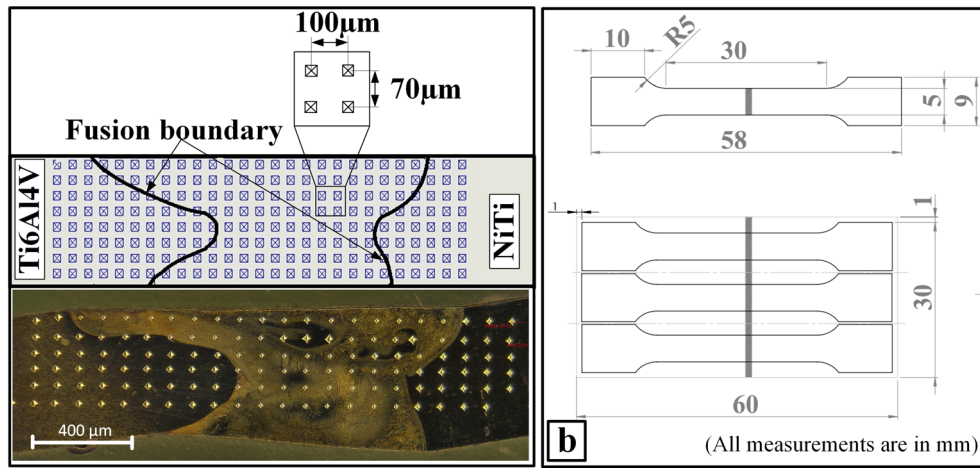


Fig. 2 Schematic of the mechanical testing specimen: (a) microhardness and (b) tensile test

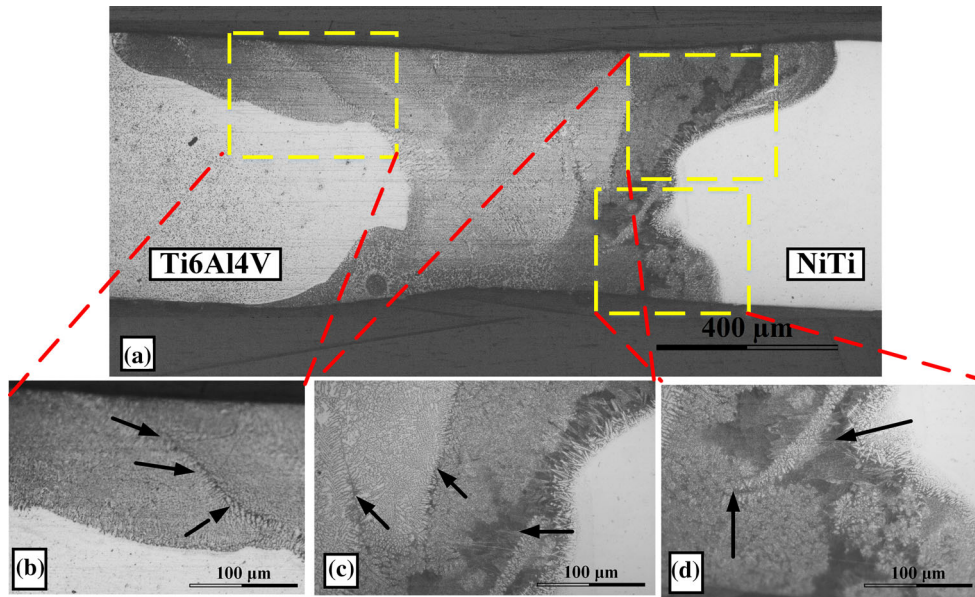


Fig. 3 (a) Micrograph of un-interlayered NiTi/Ti6Al4V dissimilar joint, (b) correspond to fusion zone toward the Ti6Al4V side and, (c) and (d) correspond to the fusion zone near the NiTi side (The black arrows indicate the interaction layer and crack initiation sites)

effect of a 50 μm thick Co interlayer on the microstructure and mechanical properties of the joint. When 30 μm Co is used, the size of the interaction layer at the NiTi boundary narrows to 11–17 μm (as shown in Fig. 4a) when compared to a joint made without an interlayer having 80–90 μm thick layer (shown in Fig. 3), resulting in a slight improvement in mechanical properties over the Co-free joint. When a 70 μm thick Co interlayer is applied, the interaction layer disappears, but the fusion between the NiTi boundary and the partially melted Co interlayer was incomplete (as shown in Fig. 4(c), resulting in a large void between the NiTi boundary and the interlayer and, as a result, a weaker joint.

The addition of the 50 μm thick Co interlayer, on the other hand, aided in the formation of defect-free joints in the FZ as a whole, with no detection of NiTi-boundary interaction layer or pores as shown in Fig. 4(b). The macrograph of the NiTi/Co/Ti6Al4V joint is further detailed in Fig. 5(a–e). Here it should be noted that the porosity observed near the Ti6Al4V fusion boundary does not have any relation with weld; it was present

in the base material before welding and revealed in the sample preparation process. Furthermore, macrosegregation was observed on NiTi/Co/Ti6Al4V dissimilar laser joint as indicated in I_1 and I_2 regions of Fig. 5(a).

As shown in Fig. 5(a), a complex solidification pattern and microstructure were evident, consisting primarily of equiaxed and columnar dendritic grains and two macrosegregated regions (indicated by I_1 and I_2). This intricate solidification pattern in dissimilar laser welding is known to be the collective result of an extremely complex fluid flow, the discrepancy in the thermophysical properties between the materials to be joined, high cooling rate, heat and mass losses, convection currents and preferentially due to the Marangoni effect (Ref 36, 37).

Attributed to the existence of a severe thermal gradient, the solidification started in a cellular manner on both NiTi and Ti6Al4V fusion boundaries as depicted in Fig. 5(b) and (c) (indicated by the black arrows). As illustrated by area ‘A’ of Fig. 5(b) (a portion of this region can be referred from Fig. 5e),

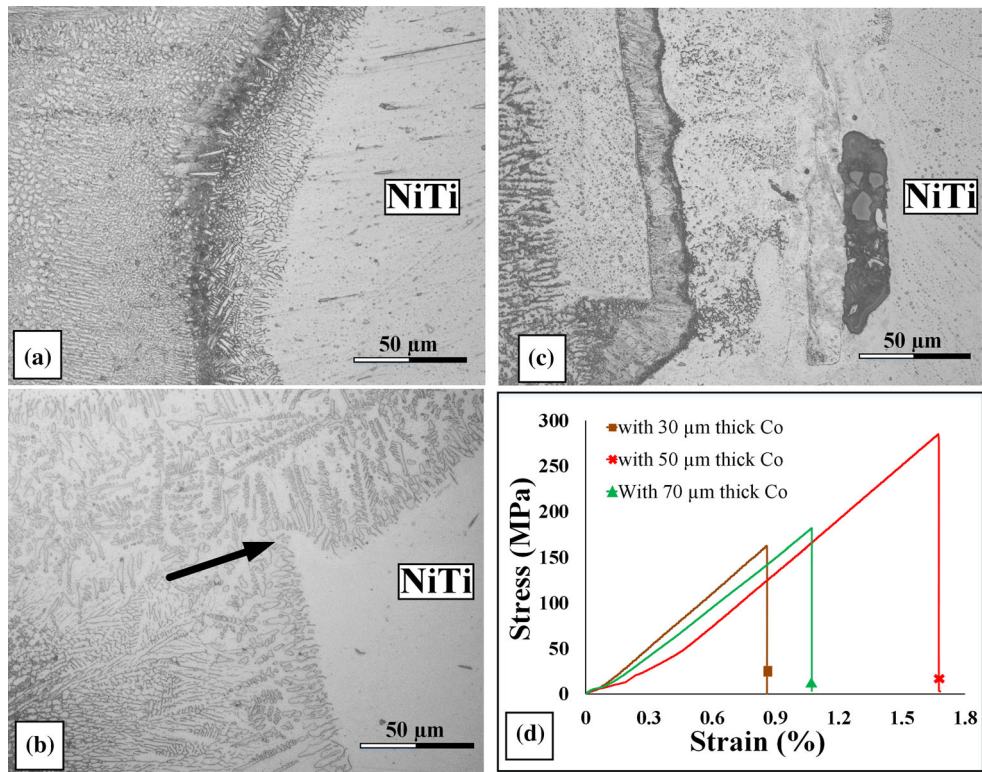


Fig. 4 Microstructure of the joints near the NiTi boundary: (a) with 30 μm thick Co, (b) with 50 μm thick Co, (c) with 70 μm thick Co, and (d) the corresponding stress-strain graphs. (The arrow in (b) shows the unevenly shaped beach observed on NiTi-FZ boundary.)

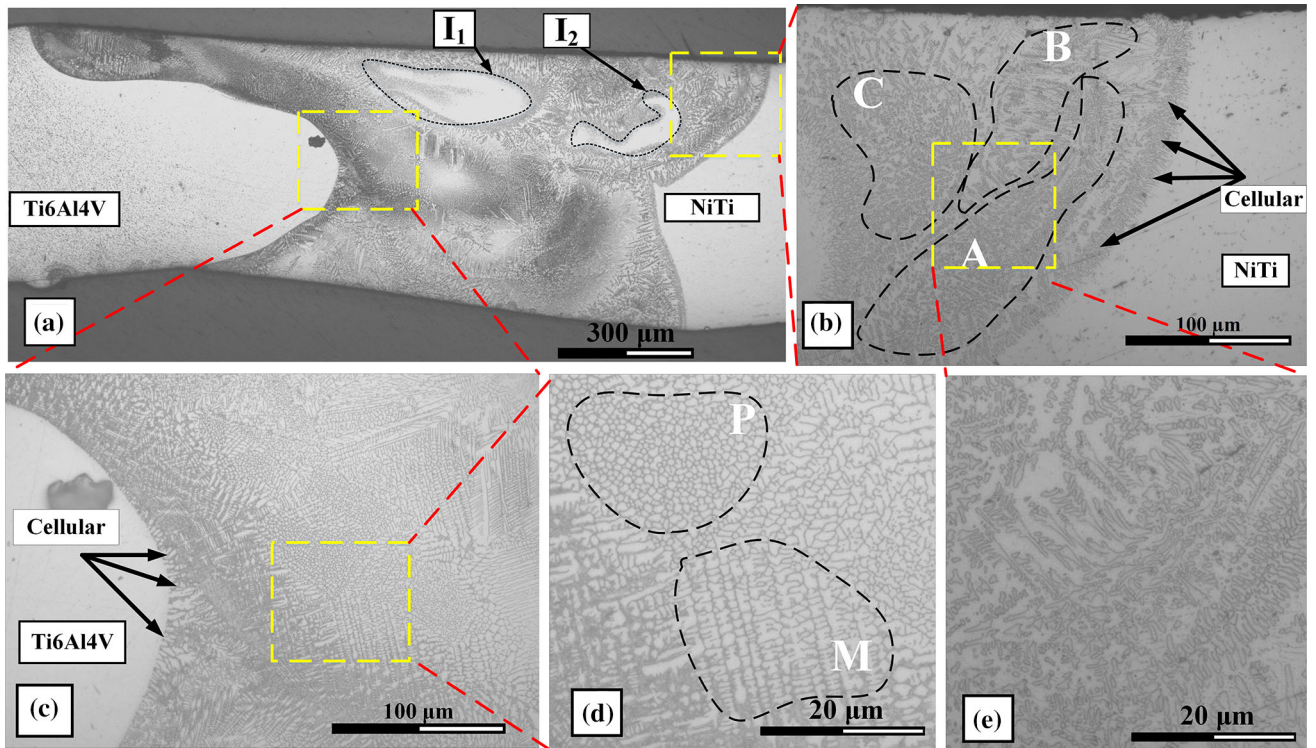


Fig. 5 (a) Micrograph of NiTi/Ti6Al4V dissimilar joint with Co interlayer, (b) NiTi boundary of weld, (c) Ti6Al4V boundary of weld (d) higher magnification near to the Ti6Al4V boundary, and (e) higher magnification near to the NiTi boundary

the cellular growth was abruptly changed to equiaxed dendrites on the NiTi side. In comparison, the cellular growth was spontaneously changed to columnar dendrites and a fine dark equiaxed structure on the Ti6Al4V side (shown by a boundary with letters 'M' and 'P' in Fig. 5d). Decrease in the thermal gradient along with the immediate cooling effect characteristic of laser welding facilitated the occurrence of undercooling, resulting in a sudden change in the solidification structure to equiaxed dendrites near the fusion boundary. Further traveling to the center of the fusion zone reveals another change in microstructure near the NiTi boundary: the columnar dendritic microstructure (marked with letter 'B' of Fig. 5b) changed to equiaxed dendrites (marked with letter 'C' of Fig. 5b). This mixed transition between microstructures could result from the continuous detachment of NiTi islands and the existence of multiple phases. A similar change in microstructure was observed in dissimilar fusion welding of Aluminum and Silicon, which was concluded to be caused by the detachment of Al islands and convection (Ref 38, 39).

Higher cooling rates and declining thermal gradient favor significant undercooling of the melt pool, aiding in the nucleation of equiaxed grains at the center of the weld (Ref 36). Typically, pulsed laser welding tends to create highly elevated temperatures for small periods of time. As time at high temperature decreases, grains will not be allowed to grow further during cooling, resulting in a fine-grained microstructure. A combined effect between laser pulsation, high cooling rate and lower temperature gradient at the center of the weld pool justifies the fine equiaxed dendritic microstructure observed at the central portion of the weld, as depicted in Fig. 6(a) without Co interlayer and (b) with Co interlayer. Similar results and conclusions were obtained during dissimilar laser welding of Ti6Al4V and NiTi (Ref 12, 36, 40).

3.1.2 Macrosegregation in Regions “I₁” and “I₂”. Macrosegregation, which is usually referred to as beaches, peninsulas and islands, can easily appear in dissimilar welding due to composition differences and subsequent variation in the local liquidus temperature. The relative difference between the liquidus temperature of mixed weld pool metal

(T_{LWM}) and liquidus temperature of base metals (T_{LBM1} and T_{LBM2}) play a vital role in the development of macrosegregation. Suppose the liquidus temperature of the mixed weld pool is lower than the liquidus temperature of the base metal ($T_{LWM} < T_{LBM1}$ and/or $T_{LWM} < T_{LBM2}$), an island of identical or nearly identical composition to the base metal is likely to occur somewhere in the weld. Alternatively, if the liquidus temperature of the mixed weld pool is higher than the liquidus temperature of the base metal ($T_{LWM} > T_{LBM1}$ and/or $T_{LWM} > T_{LBM2}$), a partially mixed island of the metal and unevenly shaped beach on the fusion boundary of lower liquidus temperature base metal are likely to occur (41). Furthermore, the literature suggests that the composition of macrosegregated regions will be similar (usually identical) to the base metals than the surrounding weld metal (Ref 36, 38, 41).

The liquidus temperature of NiTi (T_{L-NiTi}) and Ti6Al4V ($T_{L-Ti6Al4V}$) alloys is 1310 and 1605 °C, respectively. With pure cobalt having a liquidus temperature (T_{L-Co}) around 1495 °C, the NiTi/Ti6Al4V dissimilar weld with Co interlayer is expected to have a liquidus temperature (T_{LWM}) between 1310 and 1605 °C. This temperature range suggests that the weld pool with mixed composition should have a liquidus temperature above NiTi and below Ti6Al4V melting points. EDS analysis performed on the islands shown in Fig. 5(a) (marked with “I₁” and “I₂” previously) revealed that they have a NiTi-like composition and subsequently have lower liquidus temperature than the weld pool.

The phenomenon responsible for the occurrence of these NiTi-like islands is explained as follows. A partially melted island from the NiTi boundary with a relatively lower temperature was conveyed to the weld pool due to the convection currents that are generated within the melt pool. Since the weld pool has a higher relative liquidus temperature, later it will solidify around the conveyed partially melted island with lower temperature. Consequently, the island might serve as a heat sink due to its lower temperature and facilitate instant solidification of a mixed composition weld pool around itself. Owing to its lower liquidus temperature NiTi-like islands will not solidify instantly but will partially mix with the weld pool and solidify before being thoroughly mixed. This phenomenon

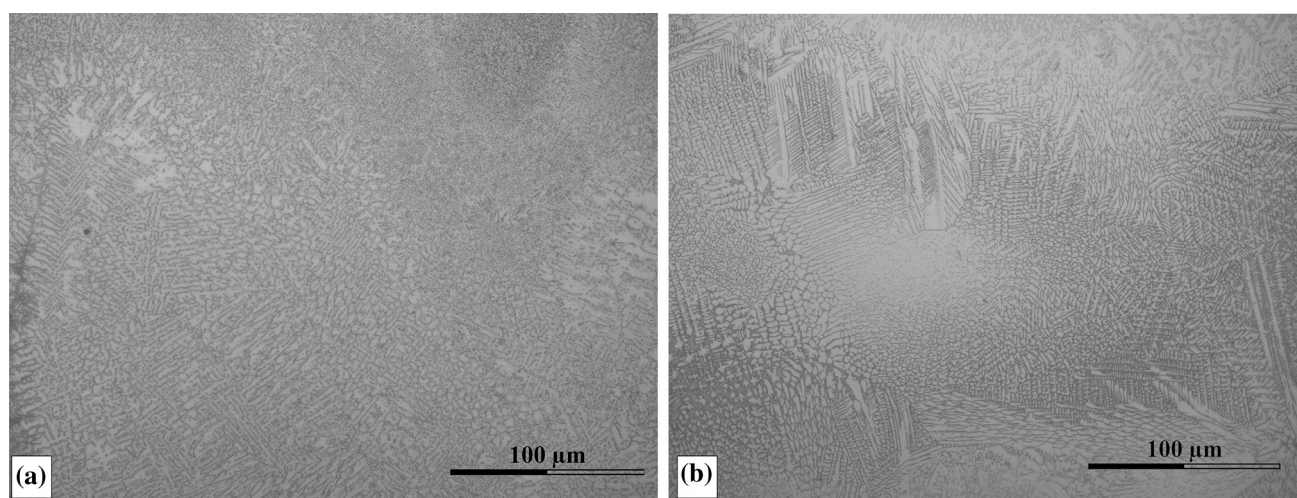


Fig. 6 Central Region micrograph of the weld (a) without Co interlayer (b) with Co interlayer

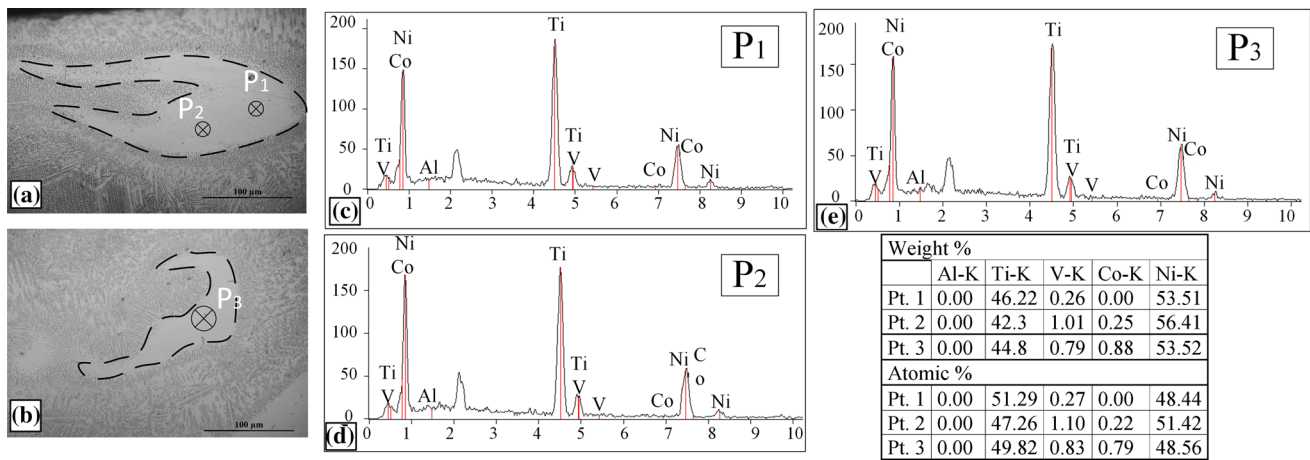


Fig. 7 Composition analysis on the NiTi-like islands observed in the center of the Co interlayer joint, (a) and (b) show locations of the test and, (c-e) show the EDS point composition analysis results

created the partially mixed NiTi islands observed in Fig. 7. A similar observation was captured when NiTi and CuAlMn were laser welded (Ref 36). As shown in Fig. 7(c-e), the SEM-EDS analysis in the macrosegregated areas revealed that the islands had a composition similar to NiTi with an element atomic percentage of ranging between 48.5 – 51.4 (Ni), 47.2 – 51.2(Ti) and a small amount of vanadium and cobalt which diffused due to the high temperatures experienced in the melt pool.

Additionally, two kinds of microstructural transitions can be observed originating from the NiTi-like islands, as shown in Fig. 7(a and b): one from cellular to dendritic and equiaxed structure, and the other from cellular to fine equiaxed and few equiaxed dendrites structure. Both transitions suggest that these islands had a lower liquidus temperature and assisted the solidification of the mixed weld-pool around themselves. Furthermore, the arrow in Fig 4(b) indicates a typical uneven shaped beach that was observed on the NiTi fusion boundary. The beach could be additional proof suggesting that a lower liquidus temperature island had been detached from the NiTi base material. Similar observations and conclusions were reached when welding NiTi to CuAlMn (Ref 36), welding aluminum to silicon (Ref 38), and welding copper to steel (Ref 41).

3.2 Compositional Changes Along the FZ

Figure 8 demonstrates the distribution of Ti, Ni, Al and Co in the joints made with and without Co interlayer. A decrease in titanium and nickel in the weld metal restrains the likelihood for Ti_2Ni to develop in the weld metal (Ref 12). The introduction of the Co interlayer resulted in an overall decrease of Ti and Ni concentration in the fusion zone. As it can be observed from Fig. 8(e), compared to Fig. 8(b), the distribution of Ti was substantially minimized throughout the weld. It was also evident from Fig. 8(c), compared to Fig. 8(f), that the distribution of Ni was slightly minimized throughout the weld and notably near the Ti6Al4V boundary. Reduction in the Ti and Ni content will reduce the tendency of these two elements to mix inside the weld pool, resulting in a lower concentration of brittle Ti_2Ni in the fusion zone.

EDS composition analysis was conducted on a $100 \times 100 \mu m^2$ central area, typically on positions shown by letters A₁ and A₂ of Fig. 9(b) and Fig. 10(b). Table 2 depicts the EDS area

composition analysis results obtained from the welds with and without the Co interlayer. These results were consistent with the overall EDS mapping depicted in Fig. 8. The area scans showed a drop in the concentration of Ti (70.23 to 59.31wt.%) on the central section of the weld. Furthermore, a noticeable increment in Co percentage was observed along with the reduction of Ti.

Further EDS point analysis was carried out on welds with and without Co interlayer to compare the compositions near the NiTi and Ti6Al4V boundaries. The results are presented in Table 3 (without Co) and Table 4 (with Co), matching the points shown in Fig. 9 and 10, respectively.

Point analysis on NiTi boundary of the weld without Co (P₃, P₄ and P₅ of Fig. 9(c and d)) and the one with Co (P₁, P₂ and P₃ of Fig. 10(a)) showed that there is a significant drop of Ti (up to 15 wt.%) and Ni (up to 6 wt.%), which was the key purpose of adding Co to the fusion zone.

Relating the EDS composition results in Table 3 with the Ti-Ni-Al ternary phase diagrams depicted in Fig. 11(a) suggest that Ti_2Ni and Ti are the primary phases to solidify in the fusion zone of the NiTi/Ti6Al4V laser welds made with an offset laser source. It is worth mentioning that offsetting the laser played a vital role in minimizing the amount of Ti_2Ni phase. Offsetting the laser to the Ti6Al4V side will reduce the melting of the NiTi base material, and the average composition of the welding pool, located at point 'O' of Fig. 11(a), will change along the 'OA' direction to a location nearby point 'C'. Consequently, the average composition will become far away from the Ti_2Ni phase region, resulting in decrease of Ti_2Ni formation in the weld pool. In addition to the laser offset, the Co interlayer added between the base materials directed the average composition along arrow 'CD' to a point near point 'D,' tending to divert the average composition further away from the Ti_2Ni phase region.

The reduction in Ni and Ti percentages and increase in Co content of the weld near the NiTi boundary suppressed the formation of microcracks observed in the NiTi/Ti6Al4V joint obtained without Co (previously depicted in Fig. 3(a, c, and d)), which should be attributed to a decrease in the concentration of brittle Ti_2Ni IMCs near the boundary. The mechanism by which Co improved the joint performance of the NiTi/Ti6Al4V dissimilar weld is as follows: when added in a controlled manner, Co is known to form shape memory alloys of the Ni-Ti-Co-system, and Co has a strong preference for entering into

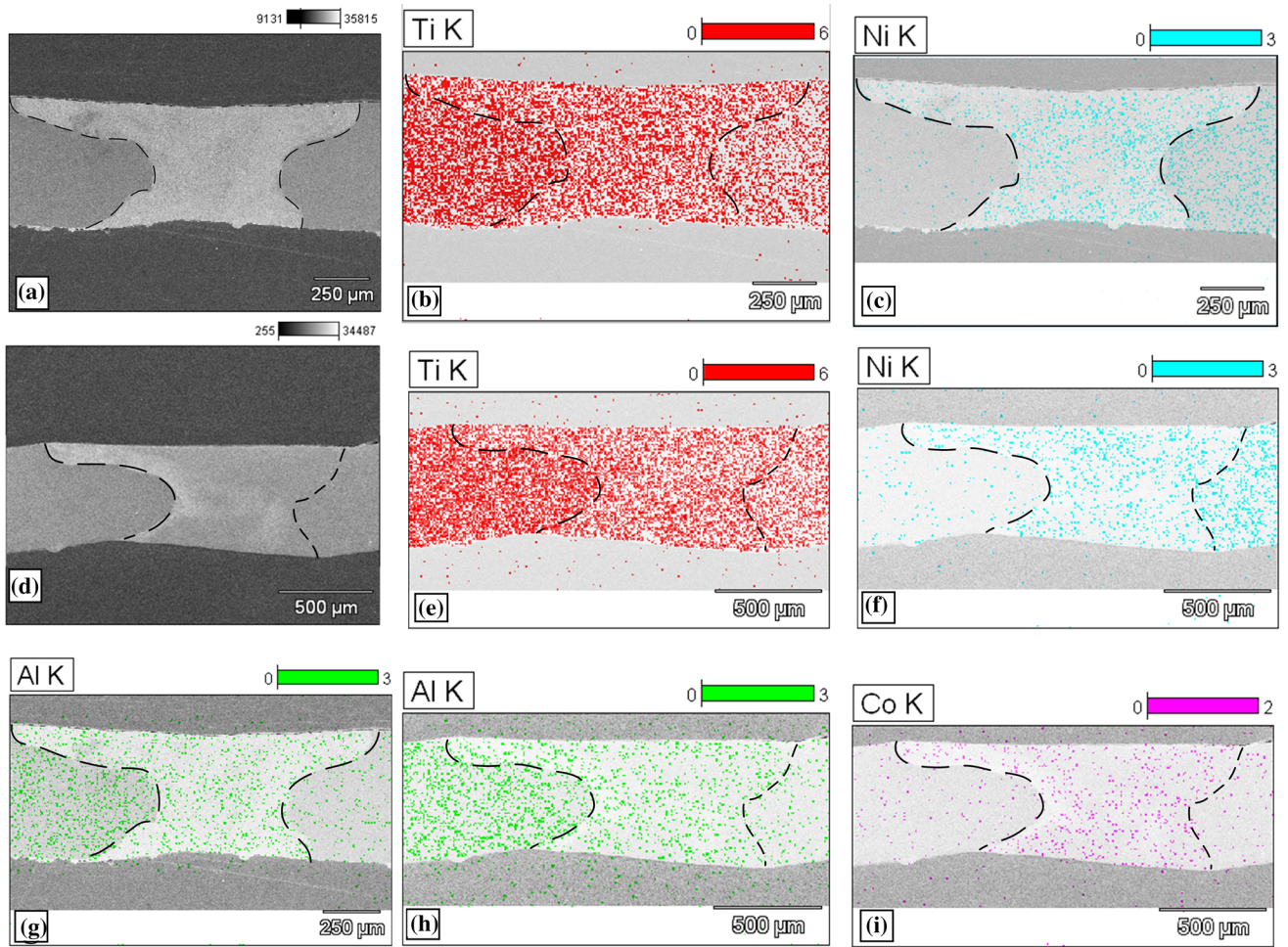


Fig. 8 EDS mapping of Ti, Ni, Al and Co in the welds ((a), (b), (c), (g) correspond to the weld without interlayer and (d), (e), (f), (h) and (i) to the weld with Co interlayer)

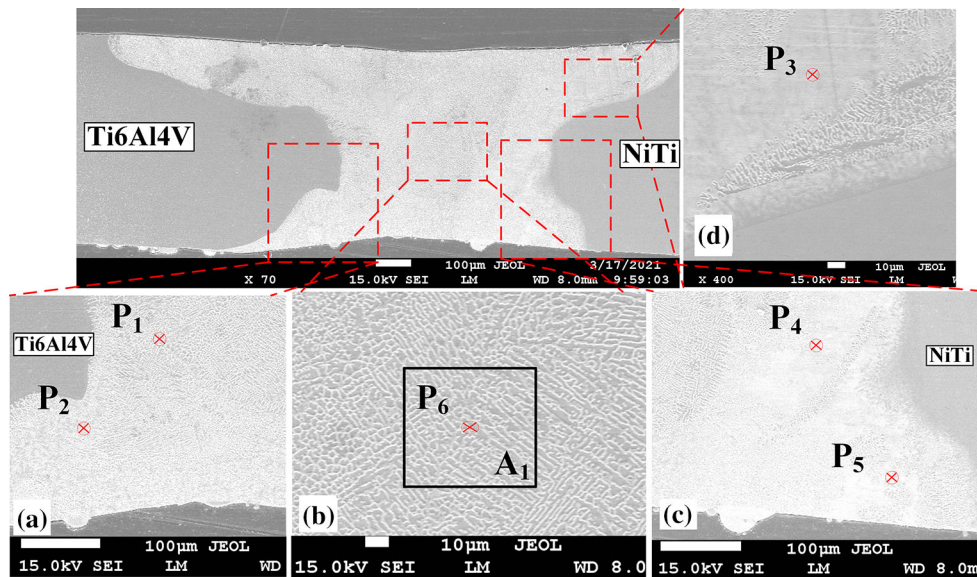


Fig. 9 Point (P1 to P7) and area (A₁) composition analysis on weld made without interlayer. (a) Ti6Al4V side (b) central of the weld (c) NiTi side

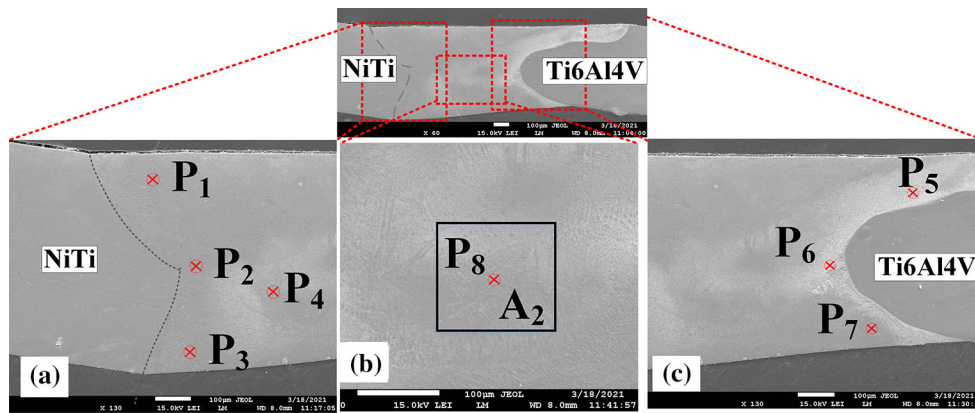


Fig. 10 Point (P1 to P8) and area (A₂) composition analysis on weld made with Co interlayer. (a) NiTi side (b) central of the weld (c) Ti6Al4V side

Table 2 EDS area (100 μm × 100 μm) composition analysis.

Area	Element weight percentage (wt.%)				
	Al-K	Ti-K	V-K	Co-K	Ni-K
A1	4.05	70.23	2.87	.	21.82
A2	2.90	59.31	3.29	12.83	21.66

Table 3 EDS point composition analysis results for the weld without Co interlayer corresponding to Fig. 9

Point	Element weight/atomic percentage (%)				Possible primary phases.
	Al-K	Ti-K	V-K	Ni-K	
P ₁	2.6	65.4/67.92	1.76	30.21/25.58	Ti ₂ Ni
P ₂	1.43	61.15/64.85	1.02	36.40/31.53	Ti ₂ Ni
P ₃	2.36	64.23/66.97	1.80	31.60/26.89	Ti ₂ Ni
P ₄	3.42	64.01/66.01	2.47	30.10/25.33	Ti ₂ Ni
P ₅	2.71	73.01/74.95	1.77	22.45/19.11	Ti ₂ Ni & Ti
P ₆	3.00	73.93/75.12	2.73	20.34/16.86	Ti ₂ Ni & Ti

Table 4 EDS point composition analysis results for the weld with Co interlayer corresponding to Fig. 10

Pt	Element weight/atomic percentage (%)					Possible primary phases.
	Al-K	Ti-K	V-K	Co-K	Ni-K	
P ₁	1.52	50.84/54.88	2.26	18.77	26.60/23.43	Ti ₂ Ni, Ti ₂ Co, NiTi
P ₂	2.62	58.63/61.67	1.70	12.65	24.40/20.94	Ti ₂ Ni, Ti ₂ Co, Ti,
P ₃	2.60	57.90/61.03	1.32	16.19	21.99/22.35	Ti ₂ Ni, Ti ₂ Co, Ti
P ₄	2.69	65.33/67.8	1.50	10.74	19.74/16.71	Ti ₂ Co, Ti ₂ Ni, Ti
P ₅	2.79	59.62/62.48	1.75	10.87	24.97/21.35	Ti ₂ Ni, Ti ₂ Co
P ₆	3.45	66.70/68.58	0.87	10.43	18.56/15.57	Ti ₂ Co, Ti ₂ Ni, Ti
P ₇	2.35	60.03/63.14	1.83	11.62	24.18/20.74	Ti ₂ Co, Ti ₂ Ni, Ti
P ₈	1.96	58.47/61.74	4.04	13.22	22.32/19.23	Ti ₂ Co, Ti ₂ Ni, Ti

the Ni sites (Ref 2, 27), which is explained by comparing the relative chemical affinity between Ti, Ni and this alloying element. In a system involving Ni-Ti and an element with

similar chemical properties to Ni, that element will tend to substitute Ni on its sites provided that the alloying element has a higher affinity to Ti. Owing to its higher chemical affinity to

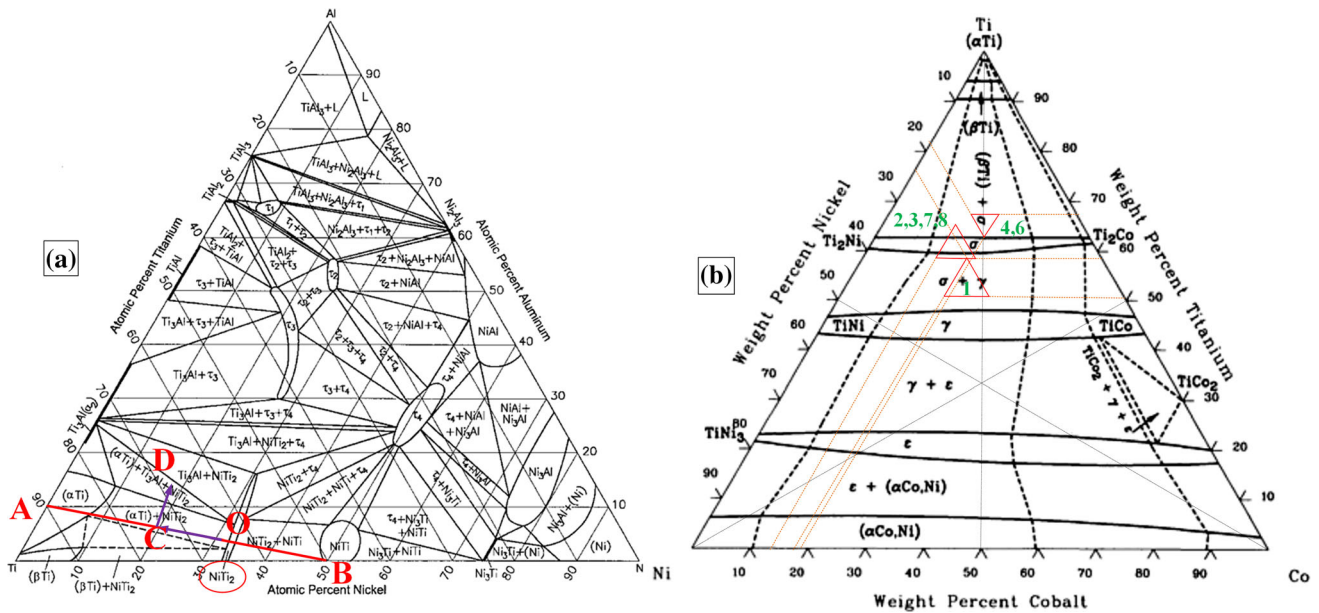


Fig. 11 Ternary phase diagrams: (a) Ti-Ni-Al (Ref 42). Reprinted from *Intermetallics*, Vol 7, B. Huneau, P. Rogl, K. Zeng, R. Schmid-Fetzer, M. Bohn, J. Bauer, “The ternary system Al–Ni–Ti Part I: Isothermal section at 900 °C; Experimental investigation and thermodynamic calculation,” Pages 1337–1345, Copyright 1999, with permission from Elsevier. (b) Ti-Ni-Co (Ref 9). Reprinted with permission of ASM International. All rights reserved. www.asminternational.org

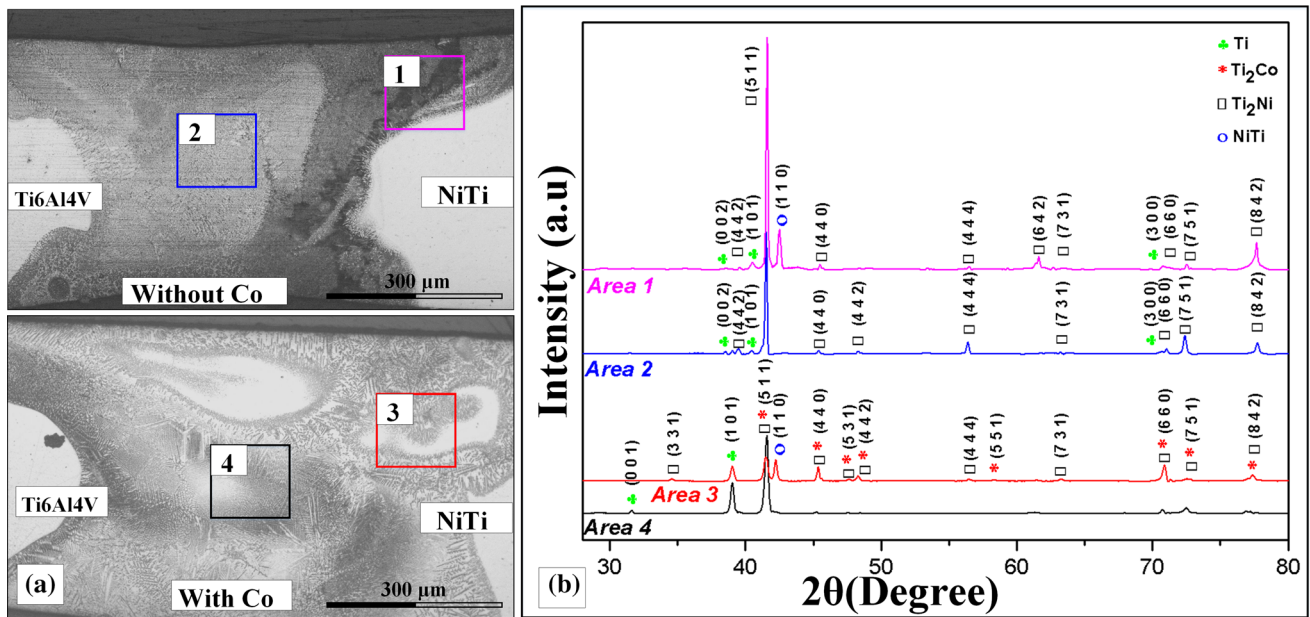


Fig. 12 Results of micro-XRD analysis. (a) approximate location of testing regions on welds with and without Co interlayer (b) micro-XRD spectra

Ti, Co could substitute for Ni irrespective of the formula of adding alloying elements (Ref 2, 26), which was evident on the Co-added NiTi/Ti6Al4V joint. When the EDS analysis results in Table 4 are matched to the Ti-Ni-Co ternary phase diagram depicted in Fig. 11(b), it appears that the addition of a Co interlayer (in addition to the offset laser) resulted in solidification of Ti_2Co , Ti_2Ni , NiTi, and Ti phases in the fusion zone. The partial substitution of Ni with Co reduced the formation of Ti_2Ni IMC and replaced a portion of it with Ti_2Co and NiTi. A

similar observation was made when welding NiTi and stainless steel with a Co interlayer (Ref 27).

Micro x-ray diffraction (XRD) analysis was used to identify the phases present in the weld at the central region of the fusion zone (which could be considered to have a fully mixed composition) and near the NiTi boundary (region with relatively higher hardness in both Co-interlayered and Co-free joints). Figure 12(b) depicts the results of the micro-XRD spectra extracted from the highlighted areas in Fig. 12(a). The micro-XRD results on the weld without a Co interlayer

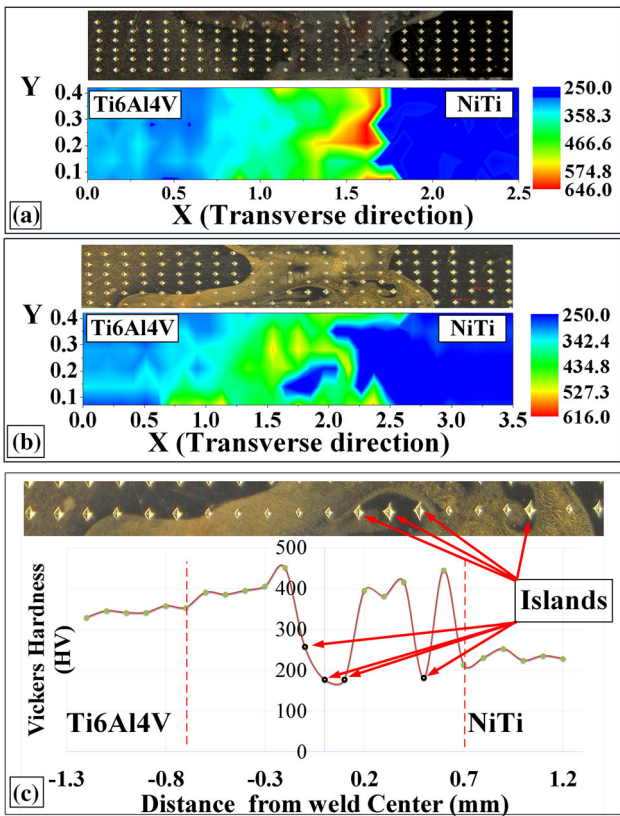


Fig. 13 Microhardness contour map. (a) without Co interlayer and (b) with Co interlayer and (c) Typical hardness testing line passing through NiTi like islands

revealed that the Ti_2Ni phase predominates in the fusion zone, with less Ti single phases. The results of a micro-XRD test on the Co-free joint near the NiTi boundary (Area 1 in Fig. 12a) and the joint center (Area 2 in Fig. 12a) revealed that the intensities corresponding to the Ti_2Ni IMC phase are larger for a testing location near the NiTi boundary (Area 1), suggesting a relatively higher concentration of Ti_2Ni there. In contrast, the XRD spectra of the weld with Co interlayer revealed that the intensities of the Ti_2Ni diffraction peaks were significantly reduced compared to the Co-free joint and detected alongside with Ti_2Co , NiTi, and Ti phases. Phases detected from micro XRD matched well with the predicted phases using EDS analysis and ternary phase diagrams.

3.3 Mechanical Properties of the Joint

3.3.1 Microhardness Mapping. The hardness map of a Ti6Al4V/NiTi joint with and without a Co interlayer is shown in Fig. 13. The microhardness of the Ti6Al4V/NiTi weld without cobalt exhibited an average (from 60 test points in the fusion zone) and maximum hardness value of 515 HV and 645 HV, respectively. The hardness measured in the fusion zone near the NiTi base material (corresponding to the interaction layer near to NiTi boundary of the Co-free joint) was the highest, and it is visible as the red zone in the hardness map depicted in Fig. 13(a). The higher hardness value of the NiTi boundary should be attributed to the relatively higher concentration of Ti_2Ni IMC near the NiTi boundary compared to the

central fusion zone (as it was evident from the micro-XRD results presented in Fig. 12b). On the other hand, the addition of the Co interlayer reduced the weld's hardness to average and maximum values of 438 and 543 HV, as shown in Fig. 13(b). Maximum hardness values were detected near the NiTi boundary in both welding conditions (Co added and Co-free) due to the relatively higher concentration of Ti_2Ni IMCs near the NiTi side (as it is evident in Fig. 12). Further from Fig. 13(c), it was evident that regions with NiTi-like islands exhibited a similar hardness with that of the NiTi base material which is in good agreement with former macrograph and previous discussion on the microstructure evolution. The hardness recorded in the FZ is significantly higher than that of the two base materials, which should be associated with the higher quantities of Ni, Ti and Co in the thoroughly mixed FZ and the resulting IMCs.

3.3.2 Effect of Co Interlayer on Tensile Properties. Figure 14(a) shows the tensile performance of Co-free and Co-added joints made with the laser offsetting method. The maximum ultimate tensile strength and fracture strain for the Co-containing joint were 285.5MPa and 1.67 %, respectively, while the Co-free joint was limited to 148MPa and 0.8 %. As shown in Fig. 14(b), all offset welds with and without Co interlayer failed near the NiTi boundary, which could be related to the hard IMCs formed near the NiTi boundary. Previous research on laser welded Ti6Al4V/NiTi joints, made by focusing the laser at the interface between the materials, concluded that high concentrations of IMCs resulted in premature joint failure even before tensile testing (Ref 11, 12). On the other hand, laser offsetting demonstrated a promising solution for partially resolving this issue by inhibiting the formation of hard and brittle IMCs. Furthermore, the addition of a Co interlayer tends to improve the joint's tensile strength and ductility by decreasing the amount of brittle Ti_2Ni formed. Co is known to increase the yield strength of Titanium and Nickel based alloys through solid solution strengthening. The atomic radius of Co (0.135 nm), Ni (0.135nm) and Ti (0.140 nm) are equivalent to each other, suggesting that the addition of Co to a Ni-Ti base alloy could result in substitutional solid solution strengthening. In this case, it is suggested that the solid solution strengthening from Co improved the mechanical properties of the NiTi/Ti6Al4V dissimilar weld. A similar solid solution strengthening effect was evident when Co is added as an alloying element in Ti- and Ni-based alloys like Ti-Al-V-Co, Ti-Pt-Co and Ni-42CrMo-steel-Co (Ref 30, 31, 43-45). Yet, the strength level reached by the laser-welded specimens was not good enough to trigger the stress-induced martensite phenomena for NiTi base material. This can be explained by the Ti_2Ni IMCs: although in less amount when Co is added to the fusion zone, their volume fraction is still high enough so that premature failure occurs during tensile testing.

Failure of the joints occurred in the FZ near the NiTi base material, which agrees with hardness map in Fig. 13, indicating that the hardness is highest near the NiTi base metal. Brittle fracture morphology with cleavage was detected on both the NiTi and Ti6Al4V sides. This fracture morphology corresponds to a brittle failure and was consistent with the nearly straight-line stress-strain relationship obtained from tensile testing. Even though cleavages made up most of the fractured surface, ductile and quasi-cleavage failure modes were also observed on the fracture morphology.

Figure 15 depicts the failure morphologies observed on the NiTi and Ti6Al4V sides of the fractured specimen. It is easy to

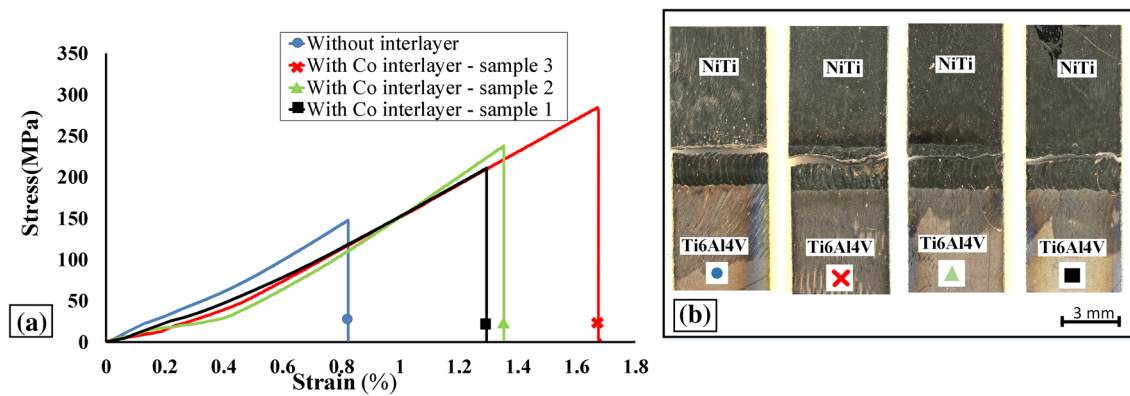


Fig. 14 (a) Stress–strain curves for Co-free and 50 μm Co interlayered Ti6Al4V/NiTi joints and (b) corresponding fractured specimens

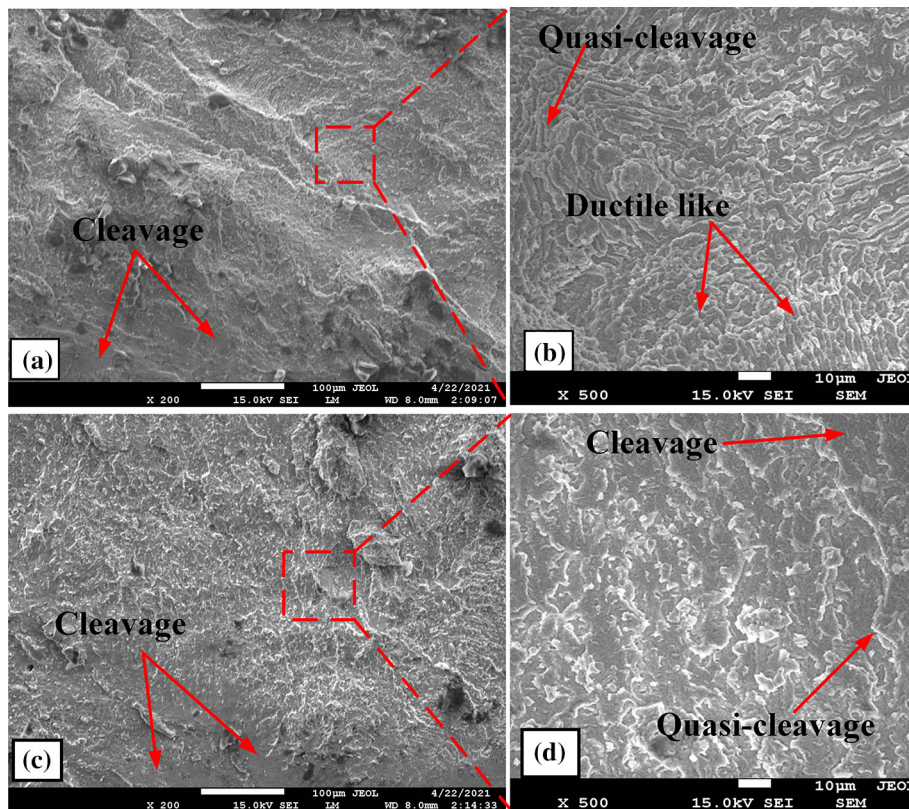


Fig. 15 SEM fracture morphology of (a) general cleavage morphology on NiTi side, (b) slight ductile and quasi cleavage behavior on NiTi side, (c) general cleavage morphology on Ti6Al4V side and, (d) quasi-cleavage behavior on Ti6Al4V side

notice a cleavage mode failure on the morphology observed on both sides of the joint, as shown in Fig. 15(a) and (c). Slight quasi-cleavage behavior was observed on both sides, as illustrated in Fig. 15(b) and (d). Figure 15(b) also shows a small area on the NiTi side with ductile-like failure behavior, which could be related to the NiTi-like islands mentioned in Fig. 5 and 7. The failure is expected to be ductile if the weld pool was entirely composed of NiTi-like islands. During tensile loading, yielding begins on the softer material, most likely the soft NiTi-like islands, which deform and transfer the load to the NiTi base material and then to the harder fusion zone, resulting in the general cleavage footprint with a minimal ductile-like

fracture shown in Fig. 15. These softer NiTi-like islands could explain the slight quasi-cleavage and ductile behavior observed on the fractured surface.

4. Conclusions

A dissimilar laser weld between Ti6Al4V and NiTi was obtained using a cobalt interlayer and laser offsetting method. The key conclusions drawn are as follows:

- Islands with a near NiTi-like composition and unevenly

shaped beaches were observed near the NiTi boundary. This phenomenon was attributed to the convection current and the FZ's higher liquidus temperature than the NiTi base metal.

- A complex and intricated microstructure was evident throughout the fusion zone, with equiaxed dendrites being vastly observed. A combined effect between laser pulsation, higher cooling rate, complexity in the material composition and lower temperature gradient at the center of the weld pool resulted in the transition of columnar to equiaxed dendrites resembling the majority of the microstructure observed in the weld.
- The use of a Co interlayer eliminated the brittle interaction layer observed on the NiTi boundary by influencing the chemical composition of the FZ and reducing the amount of Ti₂Ni.
- The addition of Co as an interlayer increased fracture strength and ductility to 285 MPa and 1.67 %, respectively, from 148 MPa and 0.8 % in joints without a Co interlayer.
- The use of the Co interlayer critically reduced the hardness of the entire weld to average and maximum values of 438 HV and 543 HV, respectively.

Acknowledgments

This work was supported by, Natural Science Foundation of China (No. 51775091), Science and Technology Project of Sichuan Province (No. 2020ZDZX0015), Guangdong Basic and Applied Basic Research Foundation (No.2021B1515140048). JPO acknowledges Fundação para a Ciência e Tecnologia (FCT) for its financial support through the project UIDB/00667/2020 (UNIDEMI). JPO acknowledges the funding of CENIMAT/i3N by national funds through the FCT-Fundação para a Ciência e a Tecnologia, I.P., within the scope of Multiannual Financing of R&D Units, reference UIDB/50025/2020-2023.

Author Contributions

FBT: Conceptualization, Writing - original draft, Methodology, and Data curation. BP: Supervision, Writing - review & editing, and Resources. JPO: Data curation, Writing - review & editing, Validation, and Resources. SA: Writing - review & editing, Validation, and Resources. WK: Data curation, Software and Writing - review & editing. FG: Software and Writing - review & editing. ZZ: Conceptualization, Supervision, Writing - review & editing, Validation and Resources. All authors have read and agreed to the published version of the manuscript.

Conflict of interest

The authors declare that they have no known competing financial interests or personal relationships that could have appeared to influence the work reported in this paper.

References

1. Z.H. Wu, D. Vokoun, C.C. Leu and C.T. Hu, A Two-Way Shape Memory Study on Ni-Rich NiTi Shape Memory Alloy by Combination

- of the All-Round Treatment and the R-Phase Transformation, *J. Mater. Eng. Perform.*, 2017, **26**(12), p 5801–5810
2. M. Mehrpouya, A. Gisario and M. Elahinia, Laser Welding of NiTi Shape Memory Alloy: A Review, *J. Manuf. Process The Society of Manufacturing Engineers*, 2018, **31**, p 162–186
3. S. Wu, X. Liu, K.W.K. Yeung, Z.S. Xu, C.Y. Chung and P.K. Chu, Wear Properties of Porous NiTi Orthopedic Shape Memory Alloy, *J. Mater. Eng. Perform.*, 2012, **21**(12), p 2622–2627
4. Z. Zeng, M. Yang, J.P. Oliveira, D. Song and B. Peng, Laser Welding of NiTi Shape Memory Alloy Wires and Tubes for Multi-Functional Design Applications, *Smart Mater. Struct.*, 2016, **25**(8), p 1–10
5. J.P. Oliveira, B. Panton, Z. Zeng, C.M. Andrei, Y. Zhou, R.M. Miranda and F.M.B. Fernandes, Laser Joining of NiTi to Ti6Al4V Using a Niobium Interlayer, *Acta Mater Elsevier Ltd*, 2016, **105**, p 9–15
6. P. Gao, B. Fan, X. Yu, W. Liu, J. Wu, L. Shi, D. Yang, L. Tan, P. Wan, Y. Hao, S. Li, W. Hou, K. Yang, X. Li and Z. Guo, Bioactive Materials Biofunctional Magnesium Coated Ti6Al4V Scaffold Enhances Osteogenesis and Angiogenesis in Vitro and in Vivo for Orthopedic Application, *Bioact. Mater.*, 2020, **5**(3), p 680–693
7. H.P. Tang, P. Zhao, C.S. Xiang, N. Liu and L. Jia, Ti-6Al-4V Orthopedic Implants Made by Selective Electron Beam Melting, *Titanium in Medical and Dental Applications*, 2018 <https://doi.org/10.1016/B978-0-12-812456-7.00011-1>
8. I. Tomashchuk, P. Sallamand, H. Andrzejewski and D. Grevey, The Formation of Intermetallics in Dissimilar Ti6Al4V/Copper/AISI 316 L Electron Beam and Nd:YAG Laser Joints, *Intermetallics, Elsevier Ltd*, 2011, **19**(10), p 1466–1473
9. H. Baker and H. Okamoto, ASM Handbook. Vol. 3. Alloy Phase Diagrams, *ASM Int. Mater. Park. Ohio 44073-0002, USA. 501*, (1992)
10. C. Li, S. Ao, J.P. Oliveira, M. Cheng, Z. Zeng, H. Cui and Z. Luo, Ultrasonic Spot Welded NiTi Joints Using an Aluminum Interlayer: Microstructure and Mechanical Behavior, *J. Manuf. Process.*, 2020, **56**, p 1201–1210
11. R.M. Miranda, E. Assunção, R.J.C. Silva, J.P. Oliveira and L. Quintino, Fiber Laser Welding of NiTi to Ti-6Al-4V, *Int. J. Adv. Manuf. Technol.*, 2015, **81**(9–12), p 1533–1538
12. A. ShojaeiZoeram and S.A.A. Akbari Mousavi, Laser Welding of Ti-6Al-4V to Nitinol, *Mater. Des.*, 2014, **61**, p 185–190
13. C. Yuhua, M. Yuqing, L. Weiwei and H. Peng, Investigation of Welding Crack in Micro Laser Welded NiTiNb Shape Memory Alloy and Ti6Al4V Alloy Dissimilar Metals Joints, *Opt. Laser Technol.*, 2017, **91**, p 197–202
14. H.C. Chen, A.J. Pinkerton and L. Li, Fibre Laser Welding of Dissimilar Alloys of Ti-6Al-4V and Inconel 718 for Aerospace Applications, *Int. J. Adv. Manuf. Technol.*, 2011, **52**(9–12), p 977–987
15. G. Thirunavukarasu and S. Kundu, High-Strength Diffusion-Bonded Joints of 17–4 Stainless Steel and T64 Alloy Using Nickel and Copper Bilayer, *J. Mater. Eng. Perform.*, 2020, **29**(1), p 515–528
16. A. Shamsolhodaei, Q. Sun, X. Wang, B. Panton, H. Di and Y.N. Zhou, Effect of Laser Positioning on the Microstructure and Properties of NiTi-Copper Dissimilar Laser Welds, *J. Mater. Eng. Perform.*, 2020, **29**(2), p 849–857
17. R.H. Shiue and S.K. Wu, Infrared Brazing Ti50Ni50 and Ti-6Al-4V Using the BAG-8 Braze Alloy, *Mater. Trans.*, 2005, **46**(9), p 2057–2066
18. A.J. Cavaleiro, A.S. Ramos, F.M. BrazFernandes, N. Schell and M.T. Vieira, Follow-up Structural Evolution of Ni/Ti Reactive Nano and Microlayers during Diffusion Bonding of NiTi to Ti6Al4V in a Synchrotron Beamline, *J. Mater. Process. Technol.*, 2020, **275**, p 116354
19. J. Xie, Y. Chen, L. Yin, T. Zhang, S. Wang and L. Wang, Microstructure and Mechanical Properties of Ultrasonic Spot Welding TiNi/Ti6Al4V Dissimilar Materials Using Pure Al Coating, *J. Manuf. Process*, 2021, **64**, p 473–480
20. H. Deng, Y. Chen, Y. Jia, Y. Pang, T. Zhang, S. Wang and L. Yin, Microstructure and Mechanical Properties of Dissimilar NiTi/Ti6Al4V Joints via Back-Heating Assisted Friction Stir Welding, *J. Manuf. Process.*, 2021, **64**, p 379–391
21. A. ShojaeiZoeram and S.A.A. Akbari Mousavi, Effect of Interlayer Thickness on Microstructure and Mechanical Properties of as Welded Ti6Al4V/Cu/NiTi Joints, *Mater. Lett.*, 2014, **133**, p 5–8
22. X.L. Gao, J. Liu and L.J. Zhang, Dissimilar Metal Welding of Ti6Al4V and Inconel 718 through Pulsed Laser Welding-Induced Eutectic

- Reaction Technology, *Int. J. Adv. Manuf. Technol.*, 2018, **96**, p 1061–1071
23. M.M. Quazi, M. Ishak, M.A. Fazal, A. Arslan, S. Rubaiee, A. Qaban, M.H. Aiman, T. Sultan, M.M. Ali and S.M. Manladan, Current Research and Development Status of Dissimilar Materials Laser Welding of Titanium and Its Alloys, *Opt. Laser Technol.*, 2020, **126**, p 106090
 24. J.P. Oliveira, R.M. Miranda and F.M. BrazFernandes, Welding and Joining of NiTi Shape Memory Alloys: A Review, *Prog. Mater. Sci.*, 2017, **88**, p 412–466
 25. P. Disegi John A, Richard Kennedy, Robert, Cobalt-Base Alloys for Biomedical Applications, *Cobalt-Base Alloys for Biomedical Applications*, J. Disegi, R. Kennedy, and R. Pilliar, Eds., (Danvers), ASTM International, (1999)
 26. K. Otsuka and X. Ren, Physical Metallurgy of Ti-Ni-Based Shape Memory Alloys, *Prog. Mater. Sci.*, 2005, **50**(5), p 511–678
 27. H. Li, D. Sun, X. Cai, P. Dong and X. Gu, Laser Welding of TiNi Shape Memory Alloy and Stainless Steel Using Co Filler Metal, *Opt. Laser Technol.*, 2013, **45**(1), p 453–460
 28. N. El-Bagoury, Microstructure and Martensitic Transformation and Mechanical Properties of Cast Ni Rich NiTiCo Shape Memory Alloys, *Mater. Sci. Technol. (United Kingdom)*, 2014, **30**(14), p 1795–1800
 29. M. Kök, H.S.A. Zardawi, I.N. Qader and M. SaitKanca, The Effects of Cobalt Elements Addition on Ti2Ni Phases Thermodynamics Parameters Crystal Structure and Transformation Temperature of NiTi Shape Memory Alloys, *Phys. J. Plus Eur.*, 2019 <https://doi.org/10.1140/epjp/i2019-12570-9>
 30. S. Tabaie, F. Rézai-Aria, B.C.D. Flipo and M. Jahazi, Dissimilar Linear Friction Welding of Selective Laser Melted Inconel 718 to Forged Ni-Based Superalloy AD730TM: Evolution of Strengthening Phases, *J. Mater. Sci. Technol.*, 2021, **96**, p 248–261
 31. K. Wang, B. Chang, Y. Lei, H. Fu and Y. Lin, Effect of Cobalt on Microstructure and Wear Resistance of Ni-Based Alloy Coating Fabricated by Laser Cladding, *Metals (Basel)*, 2017, **7**(12), p 551
 32. P. Balakrishnan, M.S. Sreekala, and S. Thomas, *Fundamental Biomaterials: Metals*, Elsevier, (2018)
 33. Z. Zeng, B. Panton, J.P. Oliveira, A. Han and Y.N. Zhou, Dissimilar Laser Welding of NiTi Shape Memory Alloy and Copper, *Smart Mater. Struct.*, 2015, **24**(12), p 125036
 34. M. Meazza and R. Rios, Merging Transition-Metal Activation and Aminocatalysis, *Synth.*, 2016, **48**(7), p 960–973
 35. S. Simões, F. Viana, A.S. Ramos, M.T. Vieira and M.F. Vieira, Reaction Zone Formed during Diffusion Bonding of TiNi to Ti6Al4V Using Ni/Ti Nanolayers, *J. Mater. Sci.*, 2013, **48**(21), p 7718–7727
 36. J.P. Oliveira, Z. Zeng, C. Andrei, F.M.B. Fernandes, R.M. Miranda, A.J. Ramirez, T. Omori and N. Zhou, Dissimilar Laser Welding of Superelastic NiTi and CuAlMn Shape Memory Alloys, *Mater. Des.*, 2017, **128**, p 166–175
 37. X. Gao, H. Liu, J. Liu and H. Yu, Laser Welding of Ti6Al4V to Cu Using a Niobium Interlayer, *J. Mater. Process. Tech.*, 2019, **270**, p 293–305
 38. Y.K. Yang and S. Kou, Macrosegregation in Al-Si Welds Made with Dissimilar Filler Metals, *Sci. Technol. Weld. Join.*, 2010, **15**(1), p 1–14
 39. M. Ghods, M. Lauer, R.N. Grugel, S.N. Tewari and D.R. Poirier, Macrosegregation Due to Convection in Al-19Cu Alloy Directionally Solidified Through an Abrupt Expansion in Cross-Section: A Comparison with Al-7Si, *J. Mater. Eng. Perform.*, 2017, **26**(10), p 4876–4889
 40. B. Kumar, S. Bag, C.P. Paul, C.R. Das, R. Ravikumar and K.S. Bindra, Influence of the Mode of Laser Welding Parameters on Microstructural Morphology in Thin Sheet Ti6Al4V Alloy, *Opt. Laser Technol.*, 2020, **131**, p 106456
 41. T. Soysal, S. Kou, D. Tat and T. Pasang, Macrosegregation in Dissimilar-Metal Fusion Welding, *Acta Mater.*, 2016, **110**, p 149–160
 42. B. Huneau, P. Rogl, K. Zeng, R. Schmid-fetzer, M. Bohn and J. Bauer, The Ternary System Al-Ni-Ti Part I: Isothermal Section at 900 °C, *Exp Invest Thermodynam Calculation, Intermetall.*, 1999, **7**(12), p 1337–1345
 43. W. Predki, A. Knopik and B. Bauer, Engineering Applications of NiTi Shape Memory Alloys, *Mater. Sci. Eng. A*, 2008, **481**, p 598–601
 44. X. Yi, H. Wang, B. Sun, K. Sun, C. Huang, Z. Gao, X. Meng, W. Cai and L. Zhao, The Microstructural Characteristics and High Temperature Mechanical Properties of Quaternary Ti–V–Al–Co Shape Memory Alloys, *J. Alloys Compd.*, 2020, **835**, p 155416
 45. A. Wadood and Y. Yamabe-Mitarai, TiPt-Co and TiPt-Ru High Temperature Shape Memory Alloys, *Sci Eng. A*, 2014, **601**, p 106–110

Publisher's Note Springer Nature remains neutral with regard to jurisdictional claims in published maps and institutional affiliations.